Geocarto International
Publication details, including instructions for authors and subscription information:
http://www.tandfonline.com/loi/tgei20

Land cover classification using Landsat 8 Operational Land Imager data in Beijing, China

Kun Jia[a], Xiangqin Wei[b], Xingfa Gu[b], Yunjun Yao[a], Xianhong Xie[a] & Bin Li[b]

[a] State Key Laboratory of Remote Sensing Science, and College of Global Change and Earth System Science, Beijing Normal University, Beijing, China

[b] Institute of Remote Sensing and Digital Earth, Chinese Academy of Sciences, Beijing, China

Accepted author version posted online: 20 Feb 2014.Published online: 31 Mar 2014.

To cite this article: Kun Jia, Xiangqin Wei, Xingfa Gu, Yunjun Yao, Xianhong Xie & Bin Li (2014) Land cover classification using Landsat 8 Operational Land Imager data in Beijing, China, Geocarto International, 29:8, 941-951, DOI: 10.1080/10106049.2014.894586

To link to this article: http://dx.doi.org/10.1080/10106049.2014.894586

Geocarto International, 2014
Vol. 29, No. 8, 941–951, http://dx.doi.org/10.1080/10106049.2014.894586

Land cover classification using Landsat 8 Operational Land Imager data in Beijing, China

Kun Jia[a], Xiangqin Wei[b]*, Xingfa Gu[b], Yunjun Yao[a], Xianhong Xie[a] and Bin Li[b]

[a]*State Key Laboratory of Remote Sensing Science, and College of Global Change and Earth System Science, Beijing Normal University, Beijing, China;* [b]*Institute of Remote Sensing and Digital Earth, Chinese Academy of Sciences, Beijing, China*

(*Received 27 November 2013; final version received 11 February 2014*)

The successful launch of Landsat 8 provides a new data source for monitoring land cover, which has the potential to significantly improve the characterization of the earth's surface. To assess data performance, Landsat 8 Operational Land Imager (OLI) data were first compared with Landsat 7 ETM + data using texture features as the indicators. Furthermore, the OLI data were investigated for land cover classification using the maximum likelihood and support vector machine classifiers in Beijing. The results indicated that (1) the OLI data quality was slightly better than the ETM + data quality in the visible bands, especially the near-infrared band of OLI the data, which had a clear improvement; clear improvement was not founded in the shortwave-infrared bands. Moreover, (2) OLI data had a satisfactory performance in terms of land cover classification. In summary, OLI data were a reliable data source for monitoring land cover and provided the continuity in the Landsat earth observation.

Keywords: land cover; classification; Landsat 8; texture; Operational Land Imager

1. Introduction

Land cover patterns reflect the underlying natural and social processes, thus providing essential information for modelling and understanding many phenomena on Earth (Liang 2008). More importantly, land cover data are important for climate change studies and understanding the complex interactions between human activities and global change (Running 2008; Gong et al. 2013). Accurate land cover information is also an essential factor for improving the performance of ecosystem, hydrologic and atmospheric models (Bounoua et al. 2002; Jung et al. 2006; Miller et al. 2007). Land cover knowledge is critical and serves as the basis for geoscience and global change studies.

Remote sensing has long been an important and effective means for monitoring land cover with its ability to quickly provide broad, precise, impartial and easily available information regarding the spatial variability of the land surface (Hansen et al. 2000; Liu et al. 2003; Thenkabail et al. 2009; Gong et al. 2013). The particular remote sensing data source is an important factor for a successful land cover classification. Landsat satellite data are commonly used remote sensing data for land cover classification (Gumma et al. 2011; Gong et al. 2013); the availability of global data-sets from Landsat has the potential to significantly improve the characterization of the earth's

*Corresponding author. Email: weixq@radi.ac.cn

land surface (Townshend et al. 2012). When Landsat 5 being decommissioned in 2013, and Landsat 7 image being missing 22% drop from the scan line corrector failure (Tollefson 2013), the successful launch of Landsat 8 on 11 February 2013 provides the continuity in the Landsat earth observation mission (Lulla et al. 2013). The Landsat 8 orbits the earth every 99 min, covering the entire earth every 16 days except for the highest polar latitudes. Landsat 8 follows a sun-synchronous orbit at an average altitude of 705 km and 98.2° inclination. The Landsat 8 sensors include an Operational Land Imager (OLI) with nine bands, including the high-resolution panchromatic band, and a Thermal Infrared Sensor (TIRS) with two thermal bands.

Compared to Landsat 7, Landsat 8 has several new features: (1) two sensors, i.e. OLI and TIRS, (2) two spectral bands that include coastal aerosol and cirrus bands, (3) one thermal band that is split into two bands, (4) a refined spectral range for some bands, improving the spectral responses across the channels, e.g. near-infrared (NIR) and panchromatic bands, (5) improved radiometric resolution from 8 bits to 12 bits (Pahlevan & Schott 2013) and (6) the change in instrument design has resulted in significant improvements in signal to noise ratios (SNR), almost twice as good as Landsat 7 (Irons et al. 2012). The narrowing of the NIR band avoids the effect of water vapour absorption at 0.825 μm, similar to that of MODIS, and helps acquire accurate surface reflectance. The enhanced radiometric resolution improves the spectral record precision and avoids spectral saturation compared to previous Landsat data. Therefore, the Landsat 8 OLI data are expected to perform better for in land cover mapping. This study is conducted to investigate the performance of Landsat 8 OLI data and demonstrate its application for land cover classification in Beijing, China.

2. Study area

Beijing, the capital of China, is located between latitudes 39°26 and 41°03′N and longitudes 115°25′E and 117°30′E, covering an area of approximately 16,800 km^2. The resident population of Beijing is approximately 19 million based on the sixth nationwide census in 2011 (Figure 1). Beijing is located in the northern extent of the North China Plain, belonging to a temperate climatic zone. The geography of Beijing is characterized by alluvial plains in the south and east with hills and mountains dominating the north, north-west and west regions. The highest point above sea level is 2303 m and the lowest is 10 m. The climate in Beijing has four distinct seasons with hot and humid summers and cold, windy and dry winters. The average annual temperature and precipitation are approximately 12 °C and 664 mm, respectively. The various land cover types, including forest, grass, cropland, developed regions and water, have made land cover classification in Beijing a representative choice. Furthermore, Beijing has undergone rapid urbanization and economic growth in recent years. As a result, the land cover has been largely changed.

3. Data and method

3.1. Data processing

Two Landsat 8 OLI data (path/row: 123/32 and 123/33) for the study area on May 12, 2013, were downloaded from the United States Geological Survey (USGS) website (http://glovis.usgs.gov/). To assess the performance of OLI data, Landsat 7 ETM + SLC-off data from May 20, 2013, (path/row, 132/32) were also downloaded from the

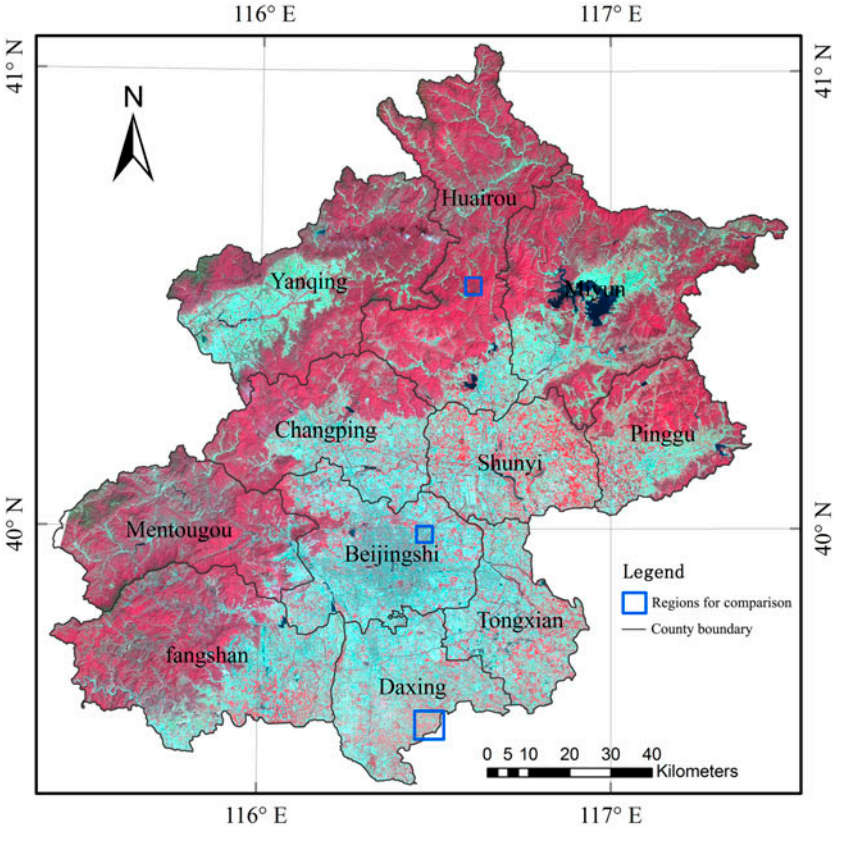

Figure 1. The geographical region of Beijing, China. The background information is the false colour image (R: NIR, G: red, B: green) of OLI data acquired on May 12, 2013. The blue rectangles show the location for assessing the data performance of OLI and ETM + data.

USGS website. It was assumed that there was no obvious land cover type change between the data acquisition time of the OLI and ETM + data. Clouds were nearly absent in the acquired Landsat data. Moreover, the quality of the multispectral data was good. Furthermore, the weather was good for the two data acquisition times and no smog appeared in the atmosphere. Therefore, it was assumed that air condition effect on the atmospheric correction of Landsat data could be ignored and there was comparability between OLI and ETM + data. Because the scan-line corrector for the ETM + sensor failed in 2003, approximately 22% of the pixels per scene were not scanned (Chen et al. 2011). Therefore, the regions selected for comparing OLI and ETM + data were located in the area where there were no data gaps in ETM + data (Figure 1).

The Landsat data processing mainly included radiance calibration, atmospheric correction, mosaic and subset. Because the continuity of the two OLI scenes was good and the co-registration between OLI and ETM + data was satisfactory through overlaying and a visual comparison, geo-referencing was not conducted in this study. The Landsat data radiance calibration converted the digital numbers value to radiance, and then atmospheric correction was performed to obtain the surface spectral reflectance using Fast Line-of-sight Atmospheric Analysis of Spectral Hypercubes (FLAASH) algorithm. FLAASH was developed to provide accurate, physics-based derivation of

atmospheric properties, which was derived from MODTRAN4, to incorporate those same quantities into a correction matrix, and finally to invert 'radiance-at-detector' measurements into the 'reflectance-at-surface' values (Cooley et al. 2002). The model selection of optical properties for ETM + and OLI data atmospheric correction using FLAASH was same to avoid the inconsistency in the corrections. Mosaic and subset data were used to extract the OLI data covering the study area for land cover classification.

3.2. *Landsat 8 OLI data compared to Landsat 7 ETM + data*

To provide a more comprehensive assessment of OLI data, the data quality was evaluated through a comparison with ETM + data using texture information contained in the data, which is a commonly used indicator for image quality (Gadkari 2004; Jiang et al. 2013). The grey-level co-occurrence matrix (GLCM) was used to extract texture features for the data comparison. The GLCM is a matrix of frequencies in which two pixels are separated using a certain vector that occurred in the image. The matrix depends on the angular and distance relationships between pixels (Haralick et al. 1973).

In this study, four features, i.e. homogeneity (HOM), contrast (CON), entropy (ENT) and angular second moment (ASM), were calculated to evaluate the data quality (Jia et al. 2012). HOM and ASM are measures of homogeneity for the image. Moreover, CON is a measure of the contrast or the amount of local variations present in an image (Haralick et al. 1973). ENT measures the disorder or complexity of an image. The ENT is large when the image is not texturally uniform and many GLCM elements have very small values. Complex textures tend to have high entropy. On one hand, HOM and ASM decrease with increasing image quality. On the other hand, CON and ENT increase with increasing image quality (Gadkari 2004). Three regions with specific main land cover classes (crop region, build-up region and forest region) were selected from the matching ETM + and OLI data to calculate the four features (Figure 1). The co-occurrence matrix values were calculated using a 3×3 window size; the grey-level value was 64 to produce the average value for each texture measurement.

3.3. *Land cover classification method*

Because ETM + data had many data gaps in the study area, it was difficult to directly compare the classification result of ETM + and OLI data. Though gaps filling methods had been developed to fill the missing regions resulted in scan line failure (Chen et al. 2011), the gaps filled image had spectral reflectance differences at a certain extent with actual situation in the data acquiring period. Direct comparison between the classification results of gaps-filled ETM + and OLI data might bring about inaccurate information. Therefore, ETM + data were not classified to compare with the classification results of OLI data in this study. Only OLI data were used for the land cover classification to assess its performance.

The maximum likelihood (MLC) and support vector machine (SVM) classifiers were selected for the land cover classification of OLI data. The MLC has been the most popular parametric classifier used for remote sensing data classification (Foody et al. 1992; Jia et al. 2011). The MLC assumes that a hyper-ellipsoid decision volume can be used to approximate the shape of the data clusters. Moreover, for a given unknown pixel, the probability of membership in each class is calculated using the mean feature

Table 1. Number of ROIs and pixels in each class type used for training and validating the MLC and SVM classifiers.

	Water	Crop	Bare land	Impervious	Forest	Grass
Number of ROIs	22	86	51	33	107	81
Number of pixels	6046	6860	7922	7046	13,390	4730

vectors of the classes, the covariance matrix and the prior probability (Duda & Hart 1973). The unknown pixel is considered to belong to the class with the maximum probability of membership. The SVM classifier is the most widely used non-parametric statistical learning classifier with no assumptions made regarding the underlying data distribution. This method typically performs better in land cover classification studies (Foody & Mathur 2004; Pal & Mather 2005; Jia et al. 2012; Pal & Foody 2012). The SVM algorithm promises to obtain the optimal separating hyper-plane for a training data-set in terms of the generalization error. A detailed description of the SVM algorithm can be found in (Burges 1998). The radial basis function (RBF), which is usually a reasonable choice (Jia et al. 2013), was selected as the kernel function for the SVM classifier. First, the RBF kernel non-linearly mapped samples into a higher dimensional space so the RBF could handle the case when the relationship between class types and attributes was not linear. Second, the RBF kernel had fewer numerical computational difficulties. The penalty value C and kernel parameter γ were the two parameters used for the RBF kernels, set to 100 and 0.167, respectively, according to prior experience. Because coastal aerosol and blue bands of the OLI data were significantly correlated and the coastal aerosol band was primarily designed for monitoring coastal waters and aerosol, the coastal aerosol band was removed in the classification process. The cirrus band, which was primarily designed for cloud identification and contained limited land surface information, was also removed for the land cover classification. Finally, surface reflectance value of bands 2, 3, 4, 5, 6 and 7 of OLI data were used for land cover classification using MLC and SVM classifier.

Based on the knowledge of land cover distribution characteristics, six classes were identified as the final class types, i.e. water, crop, bare land, impervious, grass and forest. Representative sample collection is the most time-consuming and essential process in land cover classification efforts. In this study, samples were randomly selected from known areas using the 'region of interest' (ROI) tools provided by ENVI version 5.0 software with the assistance of ground knowledge and the Google Earth tool to recognize the land cover type. Table 1 summarizes the characteristics of the sample ROIs for training and validating the classifiers. These homogeneous sample areas were easily visually identified on the OLI image and Google Earth map. The distribution of the sample pixels was uniform, well representing the entire study area. Half of the sample pixels were randomly selected as training samples, and the remaining half was used for classification accuracy assessment.

3.4. Classification accuracy assessment

To validate the land cover classification performance using OLI data, the classification results using the MLC and SVM classifiers were assessed via visual observations and quantitative classification accuracy indicators. Randomly selected sample pixels, as described in section 3.3, were used to quantitatively assess the land cover classification

accuracy. The total sample pixels used for the classification accuracy estimation were 3023 pixels for water, 3430 pixels for crop, 3961 pixels for bare land, 3523 pixels for impervious, 6695 pixels for forest and 2365 pixels for grass. The overall classification accuracy, producer's accuracy, user's accuracy and Kappa statistics were then estimated for quantitative classification performance analysis (Congalton & Green 1999; Tso & Mather 2001; Foody 2009; Foody 2013).

4. Results

4.1. Comparison between Landsat 8 OLI data and Landsat 7 ETM + data

The four average texture features (HOM, CON, ENT and ASM) in the three selected regions for comparison between OLI and ETM + data are shown in Table 2. Nearly all HOM and ASM average values for OLI VIS-NIR bands in the three regions were smaller than those for the ETM + data. Especially, the difference in HOM and ASM values between ETM + and OLI in NIR bands was large than for the VIS bands. However, the HOM and ASM average values for the SWIR bands demonstrated different performances in different regions. In crop and build-up regions, the HOM and ASM values for the SWIR bands of the OLI data were larger than for the ETM + data; the opposite was found in the forest region. As for the CON and ENT features, nearly all values for the VIS-NIR bands of the OLI data were larger than for the ETM + data. Similarly, the CON and ENT average values for the SWIR bands exhibited had different performances in different regions.

4.2. Land cover classification of OLI data in Beijing

The land cover classification results of the OLI data using the MLC and SVM classifiers are shown in Figure 2. Visually, each class type can be identified using the MLC

Table 2. Four texture features (i.e. HOM, CON, ENT and ASM) calculated in three selected regions for comparison between Landsat 7 ETM + and Landsat 8 OLI data.

		HOM		CON		ENT		ASM	
	Band	L7	L8	L7	L8	L7	L8	L7	L8
Crop region	Blue	0.214	0.202	31.492	39.018	2.080	2.085	0.118	0.118
	Green	0.188	0.169	39.889	54.846	2.090	2.102	0.117	0.115
	Red	0.170	0.150	49.989	71.965	2.103	2.111	0.115	0.113
	NIR	0.276	0.236	18.238	28.803	2.025	2.067	0.129	0.121
	SWIR 1	0.240	0.244	23.778	23.280	2.062	2.059	0.122	0.123
	SWIR 2	0.215	0.303	30.896	13.505	2.079	2.008	0.119	0.132
Build-up region	Blue	0.304	0.267	15.275	21.208	1.977	2.011	0.127	0.121
	Green	0.319	0.281	13.381	18.758	1.958	1.994	0.131	0.124
	Red	0.251	0.240	23.616	24.998	2.024	2.028	0.119	0.118
	NIR	0.284	0.205	17.096	36.809	1.996	2.053	0.124	0.114
	SWIR 1	0.271	0.320	20.275	13.052	2.002	1.957	0.123	0.131
	SWIR 2	0.262	0.324	21.541	12.555	2.007	1.951	0.122	0.132
Forest region	Blue	0.287	0.270	19.311	29.623	1.916	1.987	0.138	0.126
	Green	0.254	0.222	24.475	33.092	1.974	2.031	0.127	0.117
	Red	0.366	0.292	13.588	25.750	1.875	1.960	0.149	0.131
	NIR	0.189	0.184	37.174	42.001	2.050	2.060	0.114	0.112
	SWIR 1	0.256	0.178	52.450	53.737	1.988	2.056	0.126	0.113
	SWIR 2	0.342	0.243	18.194	29.955	1.916	2.005	0.139	0.122

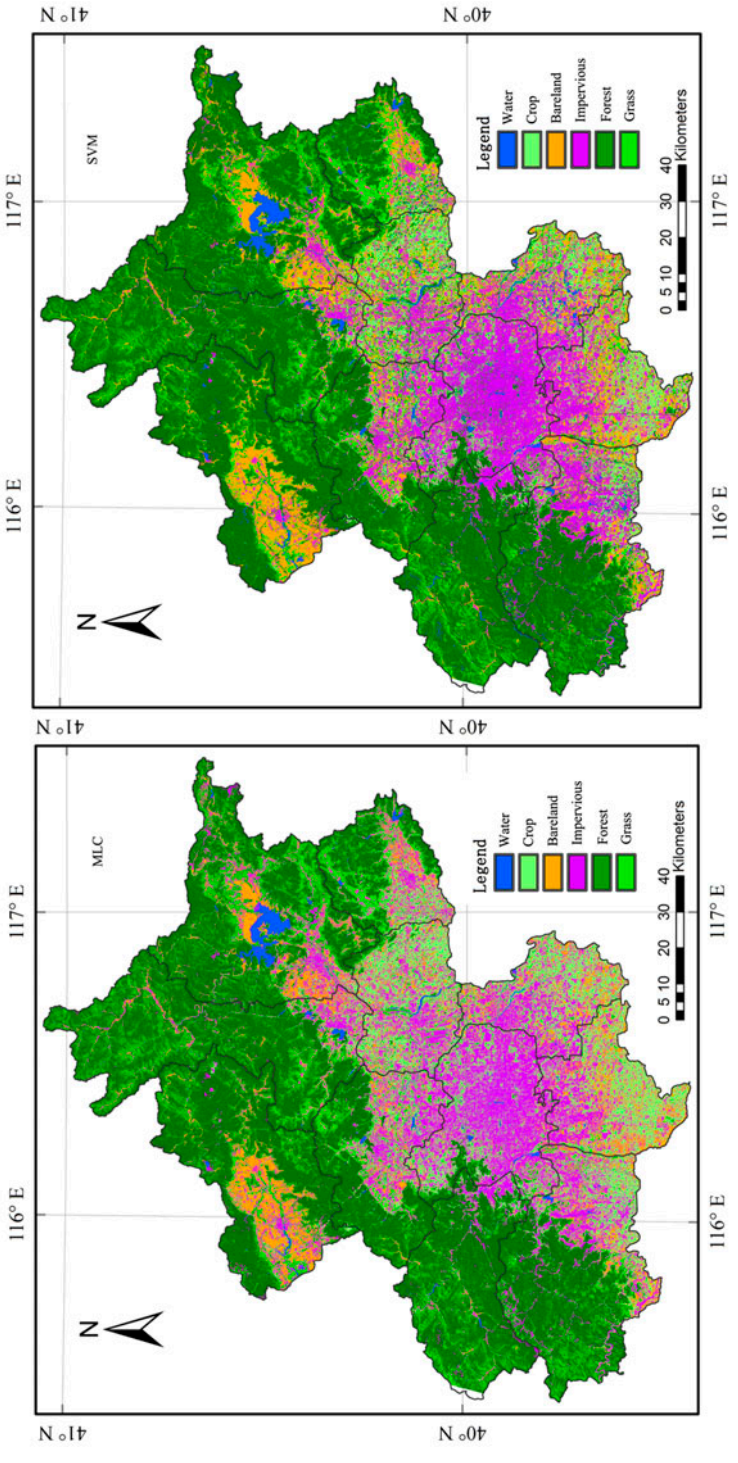

Figure 2. Land cover classification results of the OLI data using the MLC (left) and SVM (right) classifiers.

Table 3. Confusion matrixes for land cover classification of the Landsat 8 OLI data using the SVM classifier.

Mapped class	Ground truth (Pixels)							User accuracy (%)
	Water	Crop	Bare land	Impervious	Grass	Forest	Total	
Water	3001	0	0	3	0	18	3022	99.3
Crop	0	3296	2	15	59	65	3437	95.9
Bare land	2	2	3774	227	2	1	4008	94.2
Impervious	12	2	185	3261	2	0	3462	94.2
Grass	0	65	0	2	1509	455	2031	74.3
Forest	8	65	0	15	793	6156	7037	87.5
Total	3023	3430	3961	3523	2365	6695	22,997	
Producer accuracy	99.3%	96.1%	95.3%	92.6%	63.8%	91.9%		

Table 4. Confusion matrixes for land cover classification of the Landsat 8 OLI data using the MLC classifier.

Mapped class	Ground truth (Pixels)							User accuracy (%)
	Water	Crop	Bare land	Impervious	Grass	Forest	Total	
Water	2927	0	0	0	0	0	2927	100.0
Crop	1	3173	14	39	43	187	3457	91.8
Bare land	0	5	3837	257	2	0	4101	93.6
Impervious	86	28	110	3223	3	15	3465	93.0
Grass	4	126	0	4	1503	372	2009	74.8
Forest	5	98	0	0	814	6121	7038	87.0
Total	3023	3430	3961	3523	2365	6695	22,997	
Producer accuracy	96.8%	92.5%	96.9%	91.5%	63.6%	91.4%		

and SVM classifiers based on an expert's knowledge. Forests and grasses were mainly distributed in the north, north-west and west mountain regions of Beijing, accounting for more than half the area of Beijing. Crops were primarily distributed in the south and east plain regions and plain regions in Yanqing County. The impervious class was primarily distributed in urban regions.

4.3. Land cover classification accuracy

The classification accuracy and kappa statistics were estimated based on the validation samples and the confusion matrix of the OLI data classification results using the SVM and MLC classifiers are shown in Tables 3 and 4, respectively. The overall classification accuracies were all greater than 90%. The overall performance of the MLC classifier (overall accuracy 90.4%; kappa coefficient: 0.88) was slightly inferior to the SVM classifier (overall accuracy: 91.3%; kappa coefficient: 0.89). The grass class had the lowest user and producer accuracy and the maximum confusion with the forest category (Tables 3 and 4). Other class types all had a better separation with each other and higher user and producer accuracies.

5. Discussion

Texture information extracted using GLCM was selected to compare OLI and ETM + data performance. The HOM and ASM values for ETM + VIS-NIR bands were larger than that of OLI data, which indicated that the ETM + data exhibited coarser texture. Moreover, the larger difference in HOM and ASM values indicated the NIR band of the OLI had much finer texture and the refined spectral range of the NIR band improved the OLI data quality. As for SWIR bands, clear improvement was not found between OLI and ETM + data. Considering the COM and ENT texture features, the larger values for the VIS-NIR bands of the OLI data demonstrated that the OLI VIS-NIR images were clearer and contained more texture information, especially for the NIR band. In general, by comparing texture features, the image performance of the Landsat 8 OLI data was slightly better than for the Landsat 7 ETM + data in the VIS bands. Moreover, the NIR band of the OLI data clearly improved, whereas clear improvement was not found for the SWIR bands. These texture comparisons revealed that the new features of OLI sensor improved data performance, especially for the NIR band which might mainly attribute the success to narrowing the band to avoid the effect of water vapour absorption at 0.825 μm. The significant enhancements in SNR of OLI sensor might be another important reason for data performance improvement.

According to visual observations and quantitative classification accuracy assessment, there were satisfactory land cover classification results for the OLI data using both the MLC and SVM classifiers. The main difference in classification results using the MLC and SVM classifiers was that some vegetation types in main urban regions were misclassified as crops using the MLC classifier, and the SVM classifier was able to correctly classify these regions. Each class type could be better separated from each other except for grass had the lowest classification accuracy. The confusion of grass and forest was mainly caused by the fact that grass always coexisted with forest and had smaller areas in the forest gaps and boundaries. In addition, dense grass might have similar spectral characters with crops (mainly wheat in this period); sparse grass typically had lower coverage, which might be confused with bare land and impervious classes. Moreover, the SVM classifier performed better than the MLC classifier in the land cover classification using OLI data, while other studies had also demonstrated that the SVM typically performed better for land cover classification (Mountrakis et al. 2011). Considering the overall performance of OLI data using both MLC and SVM classifier, classification accuracy all exceeded 90%. Compared to the other studies, such as the land cover/use classification in Beijing using Landsat achieved overall accuracy from 87.17% to 89.23% (Wu et al. 2006), and global land cover map using Landsat TM/ETM + data with SVM classifier achieved overall accuracy of 66.63% in China (Gong et al. 2013), the classification result of OLI data is satisfactory. It was therefore indicated that OLI data had a satisfactory performance in land cover classification, and provided the reliable data continuity in the Landsat earth observation.

Overall, OLI data had a better performance compared to ETM + data and achieved satisfactory land cover classification results in this study. However, only the VIS-NIR and SWIR bands of the OLI data were investigated. Further studies might focus on evaluating the performance of the coastal aerosol band for coastal waters and aerosol monitoring, cirrus band for cloud identification and TIRS sensor thermal data for land surface temperature retrievals.

6. Conclusion

Landsat 8, the new generation of Landsat series satellites, was successfully launched and began to supply data for the worldwide community of researchers and educators in May 2013. To assess the data performance, Landsat 8 OLI data were first compared with Landsat 7 ETM + data using texture features; OLI data were also investigated for land cover classification in Beijing, China. By comparing the texture information contained in the OLI and ETM + data, and analysis of land cover classification performance using OLI data, the following primary conclusions were drawn. (1) The OLI data performance was slightly better than the ETM + data performance in the VIS bands, especially for the NIR band of the OLI data, where a clear improvement was found. Clear improvement was not founded in the SWIR bands. (2) OLI data had a satisfactory performance in land cover classification; the overall classification accuracy using the SVM classifier was higher than for the MLC classifier.

Acknowledgements

The authors thank the USGS for providing the Landsat data. The authors are very grateful for supports and assistances provided by Prof. Shunlin Liang of the Department of Geographical Sciences, University of Maryland. This study was partially funded by the National Natural Science Foundation of China (41301353), the Fundamental Research Funds for the Central Universities and the Science and Technology Subsidies to Leading Scientists by National Administration of Surveying, Mapping and Geoinformation.

References

Bounoua L, DeFries R, Collatz GJ, Sellers P, Khan H. 2002. Effects of land cover conversion on surface climate. Climatic Change. 52: 29–64.

Burges CJC. 1998. A tutorial on support vector machines for pattern recognition. Data Mining and Knowledge Discovery. 2: 121–167.

Chen J, Zhu XL, Vogelmann JE, Gao F, Jin SM. 2011. A simple and effective method for filling gaps in Landsat ETM+ SLC-off images. Remote Sensing of Environment. 115: 1053–1064.

Congalton RG, Green K. 1999. Assessing the accuracy of remotely sensed data: principles and practices. Florida: Lewis Publishers.

Cooley T, Anderson GP, Felde GW, Hoke ML, Ratkowski AJ, Chetwynd JH, Gardner JA, Adler-Golden SM, Matthew MW, Berk A, Bernstein LS, Acharya PK, Miller D, Lewis P. 2002. FLAASH, a MODTRAN4-based atmospheric correction algorithm, its application and validation. In: Proceedings of IEEE International Geoscience and Remote Sensing Symposium; Toronto, 1414–1418.

Duda RO, Hart PE. 1973. Pattern classification and scene analysis. New York, NY: Wiley.

Foody GM. 2009. Classification accuracy comparison: hypothesis tests and the use of confidence intervals in evaluations of difference, equivalence and non-inferiority. Remote Sensing of Environment. 113: 1658–1663.

Foody GM. 2013. Ground reference data error and the mis-estimation of the area of land cover change as a function of its abundance. Remote Sensing Letters. 4: 783–792.

Foody GM, Mathur A. 2004. A relative evaluation of multiclass image classification by support vector machines. IEEE Transactions on Geoscience and Remote Sensing. 42: 1335–1343.

Foody GM, Campbell NA, Trodd NM, Wood TF. 1992. Derivation and applications of probabilistic measures of class membership from the maximum-likelihood classification. Photogrammetric Engineering and Remote Sensing. 58: 1335–1341.

Gadkari D. 2004. Image quality analysis using GLCM. Orlando (FL): University of Central Florida.

Gong P, Wang J, Yu L, Zhao YC, Zhao YY, Liang L, Niu ZG, Huang XM, Fu HH, Liu S, Li CC, Li XY, Fu W, Liu CX, Xu Y, Wang XY, Cheng Q, Hu LY, Yao WB, Zhang H, Zhu P, Zhao ZY, Zhang HY, Zheng YM, Ji LY, Zhang YW, Chen H, Yan A, Guo JH, Wang L, Liu XJ, Shi TT, Zhu MH, Chen YL, Yang GW, Tang P, Xu B, Giri C, Clinton N, Zhu ZL, Chen J, Chen J. 2013. Finer resolution observation and monitoring of global land cover: first mapping results with Landsat TM and ETM+ data. International Journal of Remote Sensing. 34: 2607–2654.

Gumma MK, Thenkabail PS, Hideto F, Nelson A, Dheeravath V, Busia D, Rala A. 2011. Mapping irrigated areas of Ghana using fusion of 30 m and 250 m resolution remote-sensing data. Remote Sensing. 3: 816–835.

Hansen MC, Defries RS, Townshend JRG, Sohlberg R. 2000. Global land cover classification at 1 km spatial resolution using a classification tree approach. International Journal of Remote Sensing. 21: 1331–1364.

Haralick RM, Shanmugam K, Dinstein I. 1973. Textural features for image classification. IEEE Transactions on Systems, Man, and Cybernetics. 3: 610–621.

Irons JR, Dwyer JL, Barsi JA. 2012. The next landsat satellite: the landsat data continuity mission. Remote Sensing of Environment. 122: 11–21.

Jia K, Wu BF, Tian YC, Zeng Y, Li QZ. 2011. Vegetation classification method with biochemical composition estimated from remote sensing data. International Journal of Remote Sensing. 32: 9307–9325.

Jia K, Li QZ, Tian YC, Wu BF, Zhang FF, Meng JH. 2012. Crop classification using multi-configuration SAR data in the North China Plain. International Journal of Remote Sensing. 33: 170–183.

Jia K, Wu BF, Li QZ. 2013. Crop classification using HJ satellite multispectral data in the North China Plain. Journal of Applied Remote Sensing. 7: 073576.

Jiang B, Liang SL, Townshend JR, Dodson ZM. 2013. Assessment of the radiometric performance of Chinese HJ-1 satellite CCD instruments. Ieee Journal of Selected Topics in Applied Earth Observations and Remote Sensing. 6: 840–850.

Jung M, Henkel K, Herold M, Churkina G. 2006. Exploiting synergies of global land cover products for carbon cycle modeling. Remote Sensing of Environment. 101: 534–553.

Liang S. 2008. Advances in land remote sensing. Dordrecht: Springer.

Liu JY, Zhuang DF, Luo D, Xiao X. 2003. Land-cover classification of China: integrated analysis of AVHRR imagery and geophysical data. International Journal of Remote Sensing. 24: 2485–2500.

Lulla K, Duane Nellis M, Rundquist B. 2013. The Landsat 8 is ready for geospatial science and technology researchers and practitioners. Geocarto International. 28: 191–191.

Miller SN, Phillip Guertin D, Goodrich DC. 2007. Hydrologic modeling uncertainty resulting from land cover misclassification. Journal of the American Water Resources Association. 43: 1065–1075.

Mountrakis G, Im J, Ogole C. 2011. Support vector machines in remote sensing: a review. ISPRS Journal of Photogrammetry and Remote Sensing. 66: 247–259.

Pahlevan N, Schott JR. 2013. Leveraging EO-1 to evaluate capability of new generation of landsat sensors for Coastal/Inland water Studies. Ieee Journal of Selected Topics in Applied Earth Observations and Remote Sensing. 6: 360–374.

Pal M, Foody GM. 2012. Evaluation of SVM, RVM and SMLR for accurate image classification with limited ground data. Ieee Journal of Selected Topics in Applied Earth Observations and Remote Sensing. 5: 1344–1355.

Pal M, Mather PM. 2005. Support vector machines for classification in remote sensing. International Journal of Remote Sensing. 26: 1007–1011.

Running SW. 2008. Climate change: ecosystem disturbance, carbon, and climate. Science. 321: 652–653.

Thenkabail PS, Biradar CM, Noojipady P, Dheeravath V, Li YJ, Velpuri M, Gumma M, Gangalakunta ORP, Turral H, Cai XL, Vithanage J, Schull MA, Dutta R. 2009. Global irrigated area map (GIAM), derived from remote sensing, for the end of the last millennium. International Journal of Remote Sensing. 30: 3679–3733.

Tollefson J. 2013. Landsat 8 to the rescue. Nature. 494: 13–14.

Townshend JR, Masek JG, Huang CQ, Vermote EF, Gao F, Channan S, Sexton JO, Feng M, Narasimhan R, Kim D, Song K, Song DX, Song XP, Noojipady P, Tan B, Hansen MC, Li MX, Wolfe RE. 2012. Global characterization and monitoring of forest cover using Landsat data: opportunities and challenges. International Journal of Digital Earth. 5: 373–397.

Tso B, Mather PM. 2001. Classification methods for remotely sensed data. London: Taylor and Francis.

Wu Q, Li H, Wang R, Paulussen J, He Y, Wang M, Wang B, Wang Z. 2006. Monitoring and predicting land use change in Beijing using remote sensing and GIS. Landscape and Urban Planning. 78: 322–333.